The practical application of 2D inversion to marine controlled source electromagnetic data

Karen Weitemeyer*, Guozhong Gao†, Steven Constable*, David Alumbaugh‡

**Scripps Institution of Oceanography,*

University of California San Diego,

La Jolla, CA. 92093-0225

†*Schlumberger-Doll Research,*

1 Hampshire St,

Cambridge, MA 02139

‡*Schlumberger,*

EMI Technology Center,

1301 S 46th St, Suite #300,

Richmond, CA 94804

(June 22, 2010)

GEO-2009-0357

Running head: ***2D Inversion of CSEM data***

ABSTRACT

We present an algorithm for the inversion of marine controlled source electromagnetic (CSEM) data which uses a two dimensional (2D) finite difference (FD) forward driver. This code is demonstrated by inverting a CSEM data set collected at Hydrate Ridge, Oregon, consisting of 25 seafloor sites recording a 5 Hz transmission frequency. The sites are located across a bathymetric high, with variations in water depth of ≈300 m along the 16 km

profile. To model this complex seafloor bathymetry accurately, the FD grid was designed by careful benchmarking using a different 2D finite element (FE) forward code. A comparison of the FE and FD forward model solutions verifies that no features in the inversion are due to inaccuracies of the FD grid. The inversion includes the local seawater conductivity–depth profile as recorded by the transmitter's conductivity-temperature-depth gauge, since seawater conductivity is known to have a significant effect on the CSEM responses. An apparent resistivity pseudosection of the CSEM data resembles the 2D inversion in general appearance. However, the inversion provides depth and geometric control of features that can not be provided by the pseudosection and eliminates artifacts generated from the pseudosection projection.

INTRODUCTION

The marine controlled-source electromagnetic (CSEM) method was first developed in the academic world to explore mid-ocean ridges (Evans et al., 1994; MacGregor et al., 1998) and to study the oceanic lithosphere (Cox et al., 1986; Chave et al., 1991; Constable and Cox, 1996). These applications used a frequency-domain technique whereby a horizontal electric dipole transmitter is towed on or close to the seafloor and seafloor receivers record the transmitted fields at various frequencies and transmitter-receiver ranges (Constable and Cox, 1996). The marine CSEM method is becoming commonplace in industry to explore for hydrocarbons (Eidesmo et al., 2002; Ellingsrud et al., 2002; Hesthammer and Boulaenko, 2005; Constable and Srnka, 2007), and the use of CSEM to detect and image seafloor gas hydrates has also shown great potential (Yuan and Edwards, 2000; Schwalenberg et al., 2005; Weitemeyer et al., 2006; Zach and Brauti, 2009; Schwalenberg et al., 2009).

The collection of CSEM data in some sense has progressed further than the development of numerical and interpretational tools (forward and inverse codes) that are necessary to analyze the data. One of the first tools available was the 1D CSEM forward modeling code of Chave and Cox (1982), which formed the basis for a 1D CSEM inversion scheme (Flosadóttir and Constable, 1996) based on OCCAM, a regularized inversion technique that seeks to find the simplest or smoothest model possible. The OCCAM code is popular because it removes the influence of model parameterization and fits the data with a minimum structure model to a given tolerance (Constable et al., 1987). However, 1D analysis of data is limited to a layered representation of the earth, which is often unrealistic, and so 2D and 3D modeling codes need to be available. Some of the first 2D CSEM modeling

codes were developed for studying mid-ocean ridges, which are fairly well approximated using 2D analysis. For example, Unsworth and Oldenburg (1995) developed a 2D forward and inverse finite element code to model mid-ocean ridges, using a subspace technique for inversion. MacGregor et al. (2001) modified the forward code of Unsworth et al. (1993) to handle realistic source-receiver geometries as well as bathymetry, and incorporated it into an OCCAM 2D inversion program of deGroot Hedlin and Constable (1990). This code was used to invert CSEM data collected at the Valu Fa mid-ocean ridge in the Lau Basin, which was until recently the only published example of a 2D CSEM inversion using real data.

Commercial application of marine CSEM generally moved from 1D to 3D modeling directly because the three dimensional nature of the source field means that a 3D algorithm is in some ways easier to implement than 2D (Constable and Srnka, 2007). In addition, CSEM 3D inversion codes can be computationally expensive – often requiring the use of massively parallel computing platforms (e.g. Commer et al., 2008) making their use impractical for geophysicists limited to workstation environments, especially when one considers fully anisotropic 3D modeling. However, most CSEM data are collected as single lines or made up of single lines (for example an array of receivers composed of crossing tow lines) making 2D analysis of individual tow lines desirable. The computational expense of 3D modeling can be reduced using a 2D approximation, and the need to discretize the model along all three axes is also removed (Hohmann, 1987; Unsworth et al., 1993). Because the source field is 3D, 2D inversion and forward modeling is sometimes referred to as "2.5D", but in this paper we will use "2D" for ease of reading and for consistency with the term "1D" modeling (which also uses a 3D source).

The finite difference (FD) and finite element (FE) methods are the two most common techniques applied to forward modeling of CSEM data (Coggon, 1971; Pridmore et al., 1981;

Unsworth et al., 1993; Newman and Alumbaugh, 1995; Abubakar et al., 2008; Mitsuhata, 2000; Li and Key, 2007; Kong et al., 2008), although there are other methods available such as the intergral equation method (e.g. SanFilipo and Hohmann, 1985; Doherty, 1988; Abubakar and Habashy, 2006; Abubakar et al., 2006). The FD method is easier to implement and compute than the FE method, but the solutions are limited by the accuracy of the orthogonal grid, especially in regions where bathymetric variations are moderate to extreme. An accurate representation of complex bathymetry or other structure can cause the entire computational grid size to increase significantly, reducing the ability to obtain a solution in a reasonable time. In these cases the FE method with unstructured meshes is preferred because it allows an accurate representation of bathymetry without propagating elements through the entire grid, and eliminates the stair step representation of bathymetry required in FD meshes.

A CSEM survey conducted at Hydrate Ridge (HR), located about 100 km offshore from Newport, Oregon, was carried out to image seafloor gas hydrate, and preliminary results are presented in Weitemeyer et al. (2006). Twenty-five seafloor electromagnetic (EM) receivers were deployed, spaced approximately 650 m apart along a 16 km east–west line. Bathymetry varies from 1200 m to 900 m, and the line coincides with Ocean Drilling Program (ODP) Leg 204 logged well sites (Tréhu et al., 2003) and a 3D seismic survey (Tréhu and Bangs, 2001). The CSEM transmitter was towed 100 m above the seafloor along the receiver profile, producing an in-line geometry between transmitter and receivers. A 5 Hz square wave of 100 A current was transmitted along a 90 m dipole (for a dipole moment of 11.5 kAm at the fundamental frequency) and was recorded by the seafloor EM receivers on two horizontal and orthogonal electric field sensors (Ag-AgCl electrodes on 10 m antennae). The CSEM

data were initially analyzed by collapsing the two components of the horizontal electric fields into a polarization ellipse whose major axis was modeled to yield an apparent resistivity using the 1D modeling code of Flosadóttir and Constable (1996). The apparent resistivities were then projected into pseudosections (Weitemeyer et al., 2006).

While this provided a quick and usable image of the heterogeneity across the line without the need for a more complicated analysis, it provided no quantitative depth estimate for the features observed in the pseudosection. Some estimates of depth were obtained using 1D inversion, but the pseudosections and seismic data display folding and faulting indicative of 2D or even 3D geologic structure, in addition to the dominant 2D nature of the north-south striking bathymetry. Thus the reliability of the 1D inversion depths are questionable. At the same time, full 3D inversion is unwarranted because the full 3D effects are not captured from a single 2D line of data. The CSEM data have been collected normal to the strike of the dominant bathymetry, which is approximately 2D, and the geologic target represented by the seismic bottom simulating reflector (associated with phase change of solid hydrate above and free gas below) is ubiquitous (Tréhu et al., 1999) in the region and by its nature follows the bathymetry. Therefore a 2D forward model and/or inversion is appropriate for analysis and provides constraints on depth and eliminates the artifacts generated by the pseudosection projection presented in Weitemeyer et al. (2006). Also, it may be shown that the CSEM method has little sensitivity to structure that is more than one quarter to one half the source-receiver spacing in the cross-line direction (Constable, 2010).

In this paper we examine the application of 2D inverse modeling to a realistic CSEM data set as exemplified by the HR data, and compare the more rigorous inversion to the simple apparent resistivity pseudosection. We use a 2D inversion code similar to the code described by Gao et al. (2008) which uses a 2.5D FD code (Abubakar et al., 2008) as the

forward driver (this FD forward and inverse code is called SLB-IC here). The third section in this paper gives a description of the SLB-IC algorithm, but first we use forward responses from an adaptive finite element 2D CSEM forward code, by Li and Key (2007) (called SIO-FE here), to benchmark the construction of a FD grid for the SLB-IC code. In this way we ensure that the FD grid is accurate enough to characterize the bathymetry in the inversion, while at the same time being fast in computing the electromagnetic field responses. Of course, one might like to use the SIO-FE code for inversion, but this is complicated to implement because the error estimator that is a core part of the adaptive finite element method utilized by the SIO-FE code relies on blocky models with large regions of constant conductivity, and would fail for the small model parameter blocks typically used for 2D inversion models (K. Key, personal communication, 2010). A more efficient FE algorithm that overcomes this shortcoming is under development and will be used in future 2D inversions (K. Key, personal communication, 2009).

FORWARD MODELING OF BATHYMETRY AND FD MESH CONSTRUCTION

The effect of topography on electromagnetic measurements has been examined in Fox et al. (1980) and Jiracek (1990), with specific attention to the marine CSEM problem presented by Li and Constable (2007). Bathymetric effects result from the conductivity contrast between seawater and the seafloor, the magnitude of the effect being dependent on transmission frequency, seabed or seafloor conductivity contrast, seawater depth, transmitter-receiver geometry, and the roughness of seafloor topography (Li and Constable, 2007). Bathymetric effects can have a significant impact on data interpretation when the predicted response

from the geologic target is small, as is the case for the HR data. We have noted that FD techniques are limited to a stair step representation of bathymetry and accurate results require many small stair steps, which increases the computational time and memory needed to solve the resulting large grids. Unstructured triangular FE codes are more attractive and flexible for simulating bathymetric effects because they allow precise representation of surfaces using a grid that can conform to any arbitrary shape without propagating cells through the entire model space (Sadiku, 2001; Li and Constable, 2007).

FE Model and FD Model Implementation

To examine the relative accuracies of the FE code of Li and Key (2007) and FD code of Abubakar et al. (2008), forward models and comparisons were made between the SIO-FE and SLB-IC forward model responses generated from the CSEM tow over the HR bathymetry profile. The geometry between the transmitter and receivers was assumed to be purely in-line (radial) and the transmitter antenna dip was assumed to be zero. A number of bathymetric half-space resistivities (0.5, 1, 2, 3, and 5 Ωm) were used to select a FD grid that adequately models the bathymetry and is useable for inversion of the HR data set.

Figure 1A shows the bathymetric profile for the in-line CSEM tow at HR with 25 receivers spanning the 16 km line. The FE and FD grids discretize the bathymetric profile differently, as shown in Figure **??**B and C. The FE mesh is able to provide a more accurate model of the bathymetry and adaptively refines around receivers and transmitters, as is evident in the figure.

The SIO-FE code requires creation of a model domain and boundary condition far away from the bathymetric effects. The bathymetry profile is about 25 km in length, and on either end of the profile an assumed constant water depth is extended out to the boundary. The distance to the boundary was ±40 km (about 89 skin depths away at 5 Hz, assuming a 1 Ωm seafloor), making the entire model space 80 km by 80 km ($y \times z$). A total of 282 transmitter positions and 25 receivers were modeled. Forty-three wavenumbers were used for the wavenumber transformation carried out by this code, logarithmically spaced from 0.0000001 to 0.9. A single frequency of 5 Hz was modeled and the primary fields were computed assuming a seawater resistivity of 0.3 Ωm. The air layer was included and assigned a resistivity of 10^8 Ωm. The actual HR transmitter altitude was used for the height of the transmitter above the bathymetry profile. The problem was solved rapidly by sending approximately 40 transmitter positions to 7 computers on a 30 node cluster of Power Mac G5 Dual 2.7GHz CPUs. It took approximately 8 hours to solve for forty transmitters, except for transmitters located near complex bathymetry, where grid refinement increases considerably and computation time increases to about 16 hours. The solutions converged in about 16-24 grid refinements per transmitter. In some cases the solutions in parts of the model appeared to be corrupted with numerical errors. For these places the models were re-run with a forced grid refinement condition. The number of nodes and elements in total varied, but one typical example was 11594 nodes and 23154 elements. For the final grid refinement, the in-line electric fields have a relative differences of less than 1% between grids.

Since the SLB-IC utilizes an optimal grid technique (see Abubakar et al, 2008) one only needs to consider a 16 km segment of the 25 km bathymetry profile, where the data were

collected; the boundary conditions are automatically taken care of. Where the bathymetry crosses a grid cell an average conductivity was assigned to that cell to take into account the seawater and the seafloor conductivity by a diagonal anisotropic material averaging formula from Keller (1964) (Abubakar et al., 2008). To decrease the memory required by the computations on a single computer only every second transmitter position was modeled, reducing the problem to about 137 transmitter positions. A result was obtained within 5 to 13 minutes depending on the grid size and resistivity.

The selection of a FD grid was first determined by computing the skin depth – the distance, δ, over which field strengths are reduced by a factor of $1/e$ in a whole-space (Ward and Hohmann, 1987). The skin depth is dependent on the resistivity of the medium and on the frequency of the source field. In the case of CSEM methods a transmitter 100 m above the seafloor is almost one skin depth away from the seafloor for a transmission frequency of 5 Hz. Skin depths in seawater (0.3 Ωm) and sediment (1 Ωm) are 122.5 m and 223.6 m respectively. An accurate solution requires the spatial increment δx and δz be small (10's of meters) compared to the wavelength ($\lambda = 2\pi\delta = 770$ m for seawater and 1405 m for sediment). A couple of different grids were tested in order to get agreement with the SIO-FE responses and in some cases a modification of the grid, by increasing the grid size or modifying the conductivities, improved the solutions, especially where the bathymetry changed significantly. The final FD grid used is shown in Figure **??**B. It has a constant discretization of 50 m in the horizontal direction and a discretization of 12.5 m in the vertical direction around the bathymetric features and 25 m to 50 m in the vertical direction outside these features. Since the boundary conditions are handled automatically by the optimal grid there is no need to discretize beyond the region of concern and so a

constant horizontal discretization suitable for HR is used. There are 331 nodes horizontally and 80 nodes vertically for the entire model space.

FE and FD forward model comparisons

A comparison with the FE and FD forward modeling results are shown in Figures 2 and 3 at two different sites (site 4 and site 17). Three different types of FD grids are shown in the comparison: (a) 100 m in the horizontal by 12.5 m in the vertical, (b) 50 m horizontal by 12.5 m vertical and (c) 50 m horizontal by 25 m vertical. The log amplitude and amplitude ratio of the SLB-IC to SIO-FE computations are plotted versus distance along the profile for all components of the in-line (radial) electromagnetic field (E_x, B_y and E_z). At the bottom of Figures 2 and 3 is the bathymetric profile, with the transmitter tow and receiver positions in the region surrounding the respective sites ($\pm$3000 m). Included in Figures 2 and 3 are histograms of the amplitude ratios of the E_x (top), B_y (middle) and E_z (bottom) components for the different FD grids considered. The histograms at site 4 have a smaller spread of ratios (from 0 to 3) as compared to site 17 (ratios from 0 to 7), likely due to the different bathymetry at each location. At site 4 (Figure 2) the FE and FD responses are similar because this site is located on relatively flat bathymetry. Large differences between the FE and FD grids occur at site 17 (Figure 3) because this site is on sloping bathymetry and the limitations of the finite difference grid become more apparent. Notice at site 17 (Figure 3) the magnetic field has closest agreement between the SIO-FE and SLB-IC (ratios close to 1), whereas the vertical electric fields have the most disagreement between the SIO-FE and SLB-IC models.

The first example (Figure 2) has very similar model results for the two approaches, with the largest difference occuring at the closest approach of the transmitter to the receiver site 4 (shaded grey in the Figure). This is expected because the FD grid is limited to interpolation of the electromagnetic fields across a grid size of 12.5 m by 50 m and cannot properly model the rapid changes near the source without using a much finer grid, while the FE code will refine the grid around the source to get as accurate a solution as possible as long as there are not any scatterers immediately adjacent to the source. Bathymetric effects in the EM responses are captured by both the FE and FD codes at -7800 m, where the transmitter first attains the target height of 100 m (shaded orange in the Figure).

Site 17 (distance $\approx$2500 m) is located on a slope dipping to the east. The horizontal electric fields are underestimated on the upslope side (west $\leq$2500 m) and are overestimated on the downslope side (east $\geq$2500 m) in the 100 m by 12.5 m grids, but for both the 50 m by 12.5 m and 50 m by 25 m grids the ratio of SLB-IC : SIO-FE is $\approx$1. The vertical electric field component has the largest errors from a poor representation of bathymetry, and is vastly improved by making the grid finer. For example, the mean percentage difference changes from 209% for the 100 m by 12.5 m grid to 14.48% for the 50 by 12.5 m grid, a significant improvement in the vertical electric field computation. The magnetic fields computed from the SIO-FE and SLB-IC are almost equal, no matter what grid is used (mean percentage difference less then 4%), which is probably due to the fact that they are perpendicular to the bathymetric profile and hence are less sensitive to the changes along the profile and are also less affected by near-surface galvanic effects such as bathymetry. However, because the two codes are so different it is hard to determine why the magnetic fields appear to be more accurate. It was quickly determined that the 50 m by 12.5 m discretization gave the better solution, with most improvement seen in the vertical electric field computation.

The 50 m by 25 m grid tended to underestimate the fields. Any differences that do occur between the FD and FE codes are amplified by a higher resistivity: observe the 5 Ωm and 1 Ωm amplitude ratio plots. The overall mean of the percentage difference between the two calculations is computed for all 25 receivers; the vertical electric fields are affected most with mean percentage difference of -2% , for the magnetic fields the mean percentage difference is -1%, and for the horizontal electric fields the mean percentage difference is just 0.3%. The differences between the FE and FD are negligible for the horizontal electric component of the EM field, so this is the component that we chose to invert for the HR data set. Ranges less than 750 m were not used for inversion due to saturation of the amplifier, and therefore inaccuracies in source representation by the FD code at short ranges are not a concern.

It is important to note that we have only considered a 5 Hz frequency, very specific to the HR case study presented; a different frequency may mean a different mesh is required for inversion of the data.

INVERSION ALGORITHM

This section gives a brief introduction to one of the several inversion algorithms in the SBL-IC and which has been used to invert not only marine CSEM data, but also data generated by the Schlumberger Deeplook-EM crosswell resistivity imaging system (Gao et al., 2008). The algorithm presented here is specially designed for large-scale marine CSEM inversion.

The code minimizes a non-linear functional

$$2\phi(\mathbf{m}) = \phi^d(\mathbf{m}) + \phi^m(\mathbf{m}) \tag{1}$$

subject to

$$\mathbf{m}_{min} \leq \mathbf{m} \leq \mathbf{m}_{max} \tag{2}$$

where ϕ^d stands for the data misfit functional and ϕ^m is the model misfit functional that is used to enforce constraints on the model in terms of how the model structure varies spatially. Usually a "smoothness" constraint is enforced within the model cost function by minimizing the spatial first or second derivatives with respect to neighboring model parameters, while occasionally blocky model structure is desired by enforcing a L_1-norm or mixed L_1-norm and L_2-norm constraint on the model parameters (Farquharson and Oldenburg, 1998). The $\mathbf{m}$ is the vector of model parameters to be solved, in this case electrical conductivity, σ, at each cell, which is forced to fall between the lower bounds $\mathbf{m}_{min}$ and upper bounds $\mathbf{m}_{max}$ during the inversion. Here, we actually parameterize $\mathbf{m}$ as the logarithm of the electrical conductivity.

It is desirable to convert the above-mentioned constrained minimization problem to a unconstrained one via some non-linear parameter transformations (Habashy and Abubakar, 2004), such as

$$c_i = \frac{1}{2} \ln\left(\frac{m_i - m^i_{min}}{m^i_{max} - m_i}\right) \tag{3}$$

where c_i is the transformed intermediate parameter for the $i-th$ model parameter m_i. Thus, we now minimize

$$2\phi(\mathbf{c}(\mathbf{m})) = \phi^d(\mathbf{c}(\mathbf{m})) + \phi^m(\mathbf{m}). \tag{4}$$

Notice that we still desire to regularize on the original model parameter $\mathbf{m}$ instead of the transformed parameter $\mathbf{c}$ while solving for $\mathbf{c}$. This is important because $\mathbf{c}$ is not a physical parameter, and if regularized could produce undesiriable artifacts in the inversion results. After $\mathbf{c}$ is obtained by solving the unconstrained minimization problem in equation 4, $\mathbf{m}$ is

obtained by the inverse non-linear transformation of equation 3.

As far as we know the approach of mixing the objective function such that the data part employs the transformed variable to enforce upper and lower bounds, while the regularization is applied to the true model parameters has never been applied before. Rather, the usual method, for example using natural log parameterization, uses the transformation in both terms such that the regularization is applied to the transformed variable rather than the true earth parameter.

The data misfit, ϕ^d, is the weighted difference between the measured data, $\mathbf{d}$, and predicted forward model response, $S(\mathbf{c})$, given by

$$\phi^d(\mathbf{m}) = \|\mathbf{W}_d \cdot (\mathbf{S} - \mathbf{d})\|. \tag{5}$$

Here $\mathbf{W}_d$ is in general a data weighting matrix made up of the estimates of the standard deviations of the noise, although some other factors such as sensitivity can be incorporated, depending on the nature of the problem. Specifically, the elements of $\mathbf{W}_d$ are constructed by the product of the error estimates and the following:

$$\mathbf{W}_{kk} = (\sum_i |\mathbf{J}^0_{ki}|^2)^{-1/2} \tag{6}$$

where i is the index for the model parameter, k is the index for the data, and $\mathbf{J}^0$ is the Jacobian matrix of the first iteration. The above weighting scheme prevents the near offset measurements from dominating in the inversion, which is especially important for marine CSEM applications.

The unconstrained minimization problem, equation 4, is solved with a Gauss-Newton minimization approach as

$$\mathbf{H}_n \cdot \mathbf{s}_n = -\mathbf{g}_n \tag{7}$$

where $\mathbf{H}$ is the Hessian matrix (a square matrix of second order partial derivatives of a function), $\mathbf{s}_n$ is the search vector along which the quadratic cost function is minimized, $\mathbf{g}_n$ is the gradient of the cost function, and n is the index for the iteration. The Hessian matrix is approximated by neglecting the second order derivative of the cost function and the non-symmetric terms:

$$\mathbf{H}_n \approx \mathbf{P}_n^T[\mathbf{J}_n^T \cdot \mathbf{W}_d^T\mathbf{W}_d \cdot \mathbf{J}_n + \lambda\mathbf{T}_n]\mathbf{P}_n \tag{8}$$

and the gradient is

$$\mathbf{g}_n = \mathbf{P}_n^T \cdot \{\mathbf{J}_n^T \cdot \mathbf{W}_d^T \cdot [\mathbf{d} - \mathbf{S}(\mathbf{c}_n)] + \lambda\mathbf{T}_n \cdot \Delta\mathbf{m}(\mathbf{c}_n)\} \tag{9}$$

where $\mathbf{J}_n$ is the Jacobian matrix with respect to $\mathbf{m}$, $\mathbf{T}_n$ is the regularization matrix, λ is the regularization parameter, $\mathbf{P}$ is a transformation sensitivity matrix given by

$$\mathbf{P} = \frac{\partial\mathbf{m}}{\partial\mathbf{c}}, \tag{10}$$

and $\Delta\mathbf{m}$ is the model difference between the current model and the reference model.

The Jacobian matrix is calculated using an adjoint method with a set of forward computations in which the roles of the receiver and transmitter are interchanged (Abubakar et al., 2008). All source excitations are solved simultaneously, providing a fast solution for the inverse problem where the solution for many source locations and orientations can be achieved by inverting the stiffness matrix only once.

The Hessian matrix is large and equation 7 is solved with an iterative technique such as conjugate gradient (CGLS), or minimal residual method MINRES for $\mathbf{s}_n$. The inversion

progresses iteratively using a "dual-control mechanism": (1) the model parameters are updated via a line search algorithm to check that the cost function is reduced at each iteration (Habashy and Abubakar, 2004); (2) if the cost function is reduced, inversion goes to the next iteration while keeping the regularization parameter λ intact; (3) if the cost function can not be reduced, the regularization parameter λ (which is set to a relatively large initial value) is reduced to check whether the cost function can be reduced; (4) if both line search and reduction in λ cannot reduce the cost function, then the inversion is terminated. To guarantee the inversion converges at a reasonable speed, the regularization parameter λ is reduced at a fixed number of iterations no matter whether the line search fails or not. The dual-control mechanism will avoid the premature termination of the inversion due to a failure of the line search and makes the inversion converge smoothly. The other criteria that terminate the inversion include: (1) the data misfit reaches a predetermined tolerance; (2) the difference between the data misfit at two successive iterates is within a predetermined small number; (3) the difference between the model parameters at two successive iterations is within a predetermined small number; (4) the total number of iterations exceeds a prescribed maximum.

The inversion code can invert for a smooth model or a blocky model depending on the regularization matrix (Farquharson and Oldenburg, 1998) and the input data may include multiple frequencies and/or multiple components of the electromagnetic fields. Examples presented in this paper use a smooth model regularization.

Figure 4 (top) shows the true model of a marine CSEM synthetic example. The sea water has a depth of 1000 m and a uniform conductivity of 3 S/m. A 100 m thick and 8000 m wide 20 Ωm resistive target is located at a depth of 2000 m below sea surface in a background seabed resisitivity of 1 Ωm. The survey frequency is 0.25 Hz. Thirty-three

in-line electrical dipole sources are deployed at 50 m above the seafloor between -8 km and 8 km in the x-direction with a 500 m spacing. Seventeen in-line seafloor electric dipole receivers spaced 1 km apart are deployed on the seafloor. The domain is discretized into 171 cells in the x-direction and 60 cells in the z direction, and the mesh size is 50 m in both directions. The water conductivity is assumed known, so the inversion domain has a total of 6840 unknowns, while the number of data is 561 – an extremely under-determined problem. The starting model for the inversion is a 1 Ωm half-space without the resistive target. The data were contaminated with 1 percent random Gaussian noise, assigned an error of 5 percent of the datum amplitude, and the inversion was concluded at a RMS error close to 1.

Figure 4 (middle) shows the inverted resistivity image for a smooth inversion with a horizontal and vertical smoothing ratio of 2 to 1. The resistive target is well recovered in the image. Small artifacts occur at the edge of the inversion boundary, and there are variations of about 0.1 Ωm near the seabed, perhaps and indication of slight over-fitting of the short-range data.

An apparent resistivity pseudosection was also generated for the same synthetic example (Figure 4, bottom) to demonstrate the merits and weakness of presenting CSEM data in this way. The pseudosection was generated in a similar fashion to Weitemeyer et al. (2006). The Dipole1D forward modeling code of Key (2009) was used to generate 1D half-space forward models of 0.3, 0.5, 1, 2, 3, 5, 10, 15, and 20 Ωm and a linear interpolation was used in between these calculated half-space resistivities with the transmitter-receiver geometries discussed above. The best fitting half-space forward models were matched to the synthetic data to convert electric field amplitudes into apparent resistivity values which were then mapped into depths by computing the midpoint between the transmitter and receiver and

projecting it downwards at 45^o from the seafloor. The pseudosection in Figure 4 (bottom) is able to provide a general pattern and indicates heterogeneity exists across the tow line, but it is unable to reproduce the resistivity of the block, and unable to provide an accurate depth extent.

INVERSION OF THE HR CSEM DATA

The 2D FD inversion code requires field data in an absolute coordinate (x,y,z) system rather than the relative coordinate system (major axis of the polarization ellipse) used previously by Weitemeyer et al. (2006), and so the data are transformed into the individual Cartesian components. The navigational parameters for the transmitter antenna's position (x,y,z) and orientation (dip and angle from geodetic north) are also required for accurate modeling of the dipole source fields. We chose to only invert the inline electric field data because it has a higher data density (every site recorded this, but magnetic and vertical electric field data were only collected at every other site). Also, based on model studies, the magnetic field data are not expected to carry a large signal due to hydrate. While the vertical electric field data are expected to have a signal due to hydrate, based on the bathymetry modeling in the previous section, we expect that an accurate FD mesh for this component would likely be prohibitively large. The real and imaginary components of the electric field are inverted rather than amplitude and phase to avoid phase wrapping, but for easier interpretation we plot the electric field data as amplitude and unwrapped phase as shown in Figure 5. The observed imaginary and real in-line electric field components were assigned an error of 5% of the datum amplitude and this was used in computing the final RMS error. The receiver positions and the transmitter navigational parameters are also plotted in Figure 5 and were used to set up the transmitter model for inversion of the HR

data set. The way the navigational parameters for the transmitter were solved is discussed in detail in Weitemeyer (2008) Chapter 5. The errors in transmitter y location are known to within an average of 4 m, for x to within an average of 8 m, and to within 1 m for z. The transmitter dip is known to within an average of 2 degrees, the angle from north is known to within an average of 0.6 degrees. Receiver positions are accurate to 5 m in x and 7 m in y. Navigational errors in transmitter position are less than 10 m for this generation of CSEM data (circa 2004), which is fairly good, and the 5% error assigned to the datum amplitude is designed to capture this source of error.

The HR data set has a total of 253 transmitter positions spaced approximately every 70 m along the CSEM tow line at a nominal transmitter altitude of 100 m. Each receiver observed about 70 transmitter positions (about 55 unsaturated transmitter positions); because of the tight spacing between receivers each transmitter position was recorded by at least four different receivers along the tow line. The amplifiers saturated at source receiver offsets less than about 750 m. The 5 Hz EM signal was recorded out to ranges of about 2500 m before the noise floor of 10^{-15}V/Am^2 dominates. The redundancy and reciprocity between transmitter and receiver allowed the data set to be reduced by taking only data recorded at every fourth transmitter position (totaling 59 transmitter positions $\approx$240 m apart). This results in 234 complex data points to be inverted, from a possible 1012 data points, decreasing inversion run time and memory requirements.

The forward modeling described in the last section guided the construction of an appropriate FD grid to maintain model accuracy during the inversion of the data. A vertical profile of seawater resistivity based on the transmitter's conductivity-temperature-depth profiler (CTD) (Figure 6) was used for the inversion because seawater resistivity has a

significant effect on CSEM responses (Constable et al., 2009; Key, 2009). The inversion domain was initialized with a single seafloor resistivity of 1 Ωm and the seawater resistivity profile. The entire model mesh extends from 0 to 2400 m in depth (z) and from -8500 m to 8000 m in x but the inversion domain is specified to be only where the transmitters and receivers are located; in this case from -8250 to 7850 m in x and from 812.5 m to 2400 m in z. This region contains both seawater and sediment, so a mask was used to also remove seawater from the inversion region and only invert for sediment conductivity (colored grey in Figure 6). A smooth model regularization matrix was used to invert from this starting model.

The 2D inversion achieved an RMS misfit of 4.73 in 22 iterations from a starting RMS of 12.03 referenced to a 5% error. The RMS misfit reduction for each iteration decreases asymptotically from iteration 1-5 and then linearly decreases from iterations 5-17 until it converges at a RMS misfit of 4.73 at iteration 22 (Figure 7). Figure 8 shows the sequential development of the inversion, and a close up of the final inversion model is shown in Figure 9. The electric field amplitude and phase data are shown in Figure 5, with both the starting model 1 Ωm (dashed line) and the final inversion output (solid line). All sites have fairly good fits to the data, except for site 6 amplitudes. The SLB-IC code allows for a "static" correction, to account for an instrument calibration error, which could be applied to obtain a better fit at site 6. However, there are no calibration problems with this instrument that we could identify, and the use of this correction introduces additional structure in the entire model that does not agree well with logs obtained from ODP Leg 204. For this reason the results without a static correction are preferred. We note that the transmitter profile starts at about -7667 m, but the inversion bound extends to -8250 m and edge effects appear to be present where there are no constraints on the model. The western

side of the profile drops below the refined bathymetry, resulting in a coarser grid and a possible lack of accuracy there. This is reflected in larger amplitude percentage differences (greater the 25%) for a total of 7 data points from sites 1, 2, and 3. A similar edge effect is observed in one data point at site 25. Within the inversion boundary and away from edge effects there are also about 10 data points (besides the 10 data points at site 6) that have amplitude differences greater than 25% (at sites 11, 13, 14, 17, and 23) and these all occur at short transmitter-receiver offsets. Phase differences greater than 20° (but less than 40°) also occur at sites 12, 15, 21, and 14 (a total of 5 data points) as well as at short transmitter-reciever offsets. About 6.4% of the data (excluding site 6 and edge effects from sites 1-3 and 25) are poorly fit by the inversion. However, the redundancy in the data (i.e. one transmitter is observed by multiple receivers) means that failure to fit a few data points does not have a large effect on the model.

A shallow conductive basin is present below sites 18-25 (A in Figure 9), and a shallow resistor is at about the depth of the BSR to the west below sites 1 to 7 (B in Figure 9). At a depth of about 1600 m in the resistivity inversion model there is evidence of resistors that may correspond with anticlines associated with folding in the accretionary prism (C in Figure 9). The resistive layer interpreted to be hydrate (to the west) is about 2.5 to 5.5 Ωm (B in Figure 9). The deep accretionary complex sediments are 2 to 7 Ωm (C in Figure 9). The resistor below site 16 is 3 Ωm (C' in Figure 9). The basin and shallow sediments are more conductive and ≈0.25 times the background resistivity of 1 Ωm (A in Figure 9). The final inversion resistivity values are consistent with resistivity well logs located in this area that have values ranging from 0.3 Ωm to 3 Ωm. (Tréhu et al., 2003).

It is interesting to observe how the inversion model develops iteration by iteration (Fig-

ure 8). The resistive layer near the seismic BSR to the west appears by iteration 4 (B in Figure 8) and remains throughout further iterations, with only slight changes to the shape and resistivity. The existence of a resistor below site 16 (C' in Figure 8) appears by iteration 8 and is coincident with an anticline observed in seismic data. Finally, the accretionary complex sediments are resistive (3 Ωm), probably due to compaction of sediment, and dominate the inversion model by iteration 3 and take general shape by iteration 6 (C in Figure 8). The shallow conductive feature below site 6 becomes evident by iteration 11 (D in Figure 8). The estimated depth of investigation for the inverted data was computed using Frèchet kernels (in 1D) for 5 Hz at a range of 3 km and the depth of sensitivity is about 1.1 km below the seafloor. Given the bathymetry this gives a maximum depth of 1900 m to 2600 m before we start to lose sensitivity, well below the anticlines that occur at about 1600 m depth (C and C' in Figure 8).

COMPARISON WITH APPARENT RESISTIVITY PSEUDOSECTION

Apparent resistivity pseudosections were derived for the HR data set by matching the magnitudes of the major axis of the polarization ellipses (Constable and Cox, 1996) to electric field responses from 1D half-space forward models (Weitemeyer et al., 2006). The apparent resistivies at each range are mapped into a depth by projecting the midpoint between the source and receiver at a 45 degree angle below the seafloor. It is unwise to interpret the depth scale quantitatively with this projection technique, and pseudosections are known to produce pant-leg features, in which surface structures are projected diagonally downwards. Nevertheless, lateral variations in apparent resistivity are meaningful and the inversion and pseudosection image are broadly consistent.

An apparent resistivity pseudosection is plotted with the SLB-IC inversion result in

Figure 9. The inversion provides a quantitative depth scale unattainable from the pseudosection approach, giving both lateral and vertical resistivity distributions. There are many similarities in spite of the fact that the pseudosection is approximate and does not include effects from bathymetry. The conductive pant leg feature observed in the pseudosection still appears but has been collapsed to a surface conductor in the inversion (D in Figure 9), confirming that it was an artifact of the pseudosection projection technique. Deeper, the inversion provides an image of the folding associated with the accretionary complex sediments (C in Figure 9), also evident in the apparent resistivity pseudosection. The resistor under site 16 is still present and the conductive basin to the east also remains (C' in Figure 9). The resistor under sites 1 to 4 is obviously present in all images, but the 2D inversion limits it to a layer (B in Figure 9) rather then the broader depth extent in the pseudosection. The lateral extent of the resistive layer to the east of site 4 (from site 1 to 8) does not appear in the apparent resistivity pseudosection because the conductive pant leg artifact dominates the pseudosection image, representing perhaps the biggest failing of the pseudosection approach in this case.

CONCLUSIONS

A 2D EM inversion code has proved effective at inverting a real marine CSEM horizontal electric field set acquired at Hydrate Ridge, offshore Oregon. Both amplitude and phase can be included in the inversion through the use of real and imaginary components of the fields. The inversion generates a model that fits the data well and contains structures that agree with the geological features expected for this area. The SLB-IC (called 2.5D Deep EM Inversion) exploits the algorithmic and computational advantages of the FD model

parameterization, at the cost of requiring a stair-step characterization of bathymetry and potential inaccuracy in the calculations as a result. However, we have been able to validate the FD mesh used for the inversion by carrying out forward model comparisons using the forward modeling FE code of Li and Key (2007). The FE code generates a mesh which conforms to bathymetry, and uses an adaptive refinement algorithm to provide good control over the accuracy of the computation. Comparisons with the FE code calculations allowed us to choose a FD mesh which provided a reasonable compromise between accuracy and computational efficiency; without this step one may have been tempted to choose a FD mesh which was too coarse to provide accurate responses.

Comparison of the 2D inversion model with an apparent resistivity pseudosection generated from the same data set shows some similarity between the two images. The average resistivities are similar, although the inversion generates a model with higher contrast between resistivity highs and lows. General features of the sedimentary structure such as folding and variations in thickness are evident in both images, and a region at the western edge of the profile interpreted as being gas hydrate also shows up as relatively resistive in both. Although some quantitative estimates of depth for features in the apparent resistivity pseudosection can be obtained by 1D inversion (Weitemeyer et al., 2006), the 2D inversion provides much better quantification of depth, and also provides tighter constraints on the depth extent of the hydrate resistor. Furthermore, there is no quantifiable depth associated with a pseudosection. Thus not only does it have problems creating an accurate image below conductive and resistive features, there is no true depth information. The most obvious improvement from carrying out the more rigorous interpretation comes from the characteristic pant-leg artifact generated by a near-surface conductor in the pseudosection; the inversion correctly models the conductor as a discrete feature at the surface, allowing

a resistive feature below to be properly expressed. An experienced interpreter would unlikely be fooled by the pant-leg feature, but the deeper resistor cannot be imaged without inversion.

That the apparent resistivity pseudosection produces such a reasonable result is probably due to the small resistivity contrasts encountered in this profile, although one might have expected the bathymetry to have a confounding influence based on our forward model studies. We conclude that, while one must be cautious in drawing quantitative conclusions from pseudosections, given their huge computational advantage they provide a useful preliminary interpretation tool, and may serve as a helpful guide in setting up the numerical inversions which will always be necessary for analysis of marine CSEM data.

ACKNOWLEDGEMENTS

Yuguo Li and Kerry Key are thanked for developing and providing the finite element forward modeling code, MARE2DCSEM, and for many useful discussions. Funding for data collection was provided by ExxonMobil and GERD, Japan. General support for KW came from the Scripps Institution of Oceanography Seafloor Electromagnetic Methods Consortium and the US Department of Energy (contract DE-NT0005668). We also thank Schlumberger for allowing us to publish the inversion results. The data set used for the inversion has been made available to the marine EM community and can be found on the Scripps Institution of Oceanography Marine Electromagnetic methods webpage at http://marinemlab/projects/HYREX04.

REFERENCES

Abubakar, A., T. Habashy, V. Druskin, L. Knizherman, and D. Alumbaugh, 2008, 2.5D forward and inverse modeling for interpreting low frequency electromagnetic measurements: Geophysics, **73**, F165–F177.

Abubakar, A. and T. M. Habashy, 2006, A closed-form expression of the electromagnetic tensor green's functions for a homogeneous TI-anisotropic medium: IEEE Geoscience and remote sensing letters, **3**, 446–451.

Abubakar, A., P. M. van den Berg, and T. M. Habashy, 2006, An integral equation approach for 2.5-dimensional forward and inverse electromagnetic scattering: Geophysical Journal International, **165**, 744–762.

Chave, A. D., S. C. Constable, and R. N. Edwards, 1991, Electrical exploration methods for the seafloor, *in* Nabighian, M., ed., Electromagnetic Methods in Applied Geophysics, chapter 12, 931–966, Society of Exploration Geophysicists.

Chave, A. D. and C. Cox, 1982, Controlled electromagnetic sources for measuring electrical conductivity beneath the oceans –I, Forward problem and model study: Journal of Geophysical Research, **87**, 5327–5338.

Coggon, J., 1971, Electromagnetic and electrical modeling by finite element method: Geophysics, **36**, 132–155.

Commer, M., G. Newman, J. Carazzone, T. Dickens, K. Green, L. Wahrmund, D. Willen, and J. Shiu, 2008, Massively parallel electrical-conductivity imaging of hydrocarbons using the IBM Blue Gene/L supercomputer: IBM Journal of Research and Developement, **52**.

Constable, S., 2010, Ten years of marine CSEM for hydrocarbon exploration: Geophysics, **in press**.

Constable, S. and C. S. Cox, 1996, Marine controlled-source electromagnetic sounding 2. The PEGASUS experiment: Journal of Geophysical Research, **101**, 5519–5530.

Constable, S., K. Key, and L. Lewis, 2009, Mapping offshore sedimentary structure using electromagnetic methods and terrain effects in marine magnetotelluric data: Geophysical Journal International, **176**, 431–442.

Constable, S. and L. J. Srnka, 2007, An introduction to marine controlled-source electromagnetic methods for hydrocarbon exploration: Geophysics, **72**, WA3–WA12.

Constable, S. C., R. Parker, and C. Constable, 1987, Occam's inversion: A practical algorithm for generating smooth models from electromagnetic sounding data: Geophysics, **52**, 289–300.

Cox, C., S. Constable, and A. Chave, 1986, Controlled-source electromagnetic sounding of the oceanic lithosphere: Nature, **320**, 52–54.

deGroot Hedlin, C. and S. Constable, 1990, Occam's inversion to generate smooth, two-dimensional models from magnetotelluric data: Geophysics, **55**, 1613–1624.

Doherty, J., 1988, EM modelling using surface integral equations: Geophysical Prospecting, **36**, 644–668.

Eidesmo, T., S. Ellingsrud, L. M. MacGregor, S. Constable, M. C. Sinha, S. Johansen, F. N. Kong, and H. Westerdahl, 2002, Sea bed logging (SBL), a new method for remote and direct identification of hydrocarbon filled layers in deepwater areas: First Break, **20**, 144–152.

Ellingsrud, S., T. Eidesmo, S. Johansen, M. Sinha, L. MacGregor, and S. Constable, 2002, Remote sensing of hydrocarbon layers by seabed logging (SBL): Results from a cruise offshore Angola: The Leading Edge, 972–982.

Evans, R., S. Constable, M. Sinha, and M. Unsworth, 1994, On the electrical nature of the

axial melt zone at 13°N on the East Pacific Rise: Journal of Geophysical Research, **99**, 577–588.

Farquharson, C. and D. Oldenburg, 1998, Non-linear inversion using general measures of data misfit and model structure: Geophysical Journal International, **134**, 213–227.

Flosadóttir, A. H. and S. Constable, 1996, Marine controlled-source electromagnetic sounding 1. Modeling and experimental design: Journal of Geophysical Research, **101**, 5507–5517.

Fox, R. C., G. W. Hohmann, T. J. Killpack, and L. Rijo, 1980, Topographic effects in resistivity and induced polarization surveys: Geophysics, **45**, 75–93.

Gao, G., D. Alumbaugh, P. Zhang, H. Zhang, C. Levesque, R. Rosthal, J. Liu, A. Abubakar, and T. Habashy, 2008, Practical implications of nonlinear practical implications of nonlinear inversion for cross-well electromagnetic data collected in cased-wells: SEG Expanded Abstracts, **27**, 299.

Habashy, T. and A. Abubakar, 2004, A general framework for constraint minimization for the inversion of electromagnetic measurements: Progress in Electromagnetics Research PIER, **46**, 265–312.

Hesthammer, J. and M. Boulaenko, 2005, The offshore EM challenge: First Break, **23**, 59–66.

Hohmann, G. W., 1987, Electromagnetic methods in applied geophysics, volume **1** *of* Investigations in Geophysics Volume 3, chapter 5: Numerical Modeling for Electromagnetic Methods of Geophysics, 313–363. Society of Exploration Geophysicists.

Jiracek, G. R., 1990, Near-surface and topographic distortions in electromagnetic induction: Surveys in Geophysics, **11**, 163–203.

Keller, J., 1964, A theorem on the conductivity of a composite medium: Journal of Math-

ematical Physics, **5**, 548–549.

Key, K., 2009, 1D inversion of multicomponent, multifrequency marine CSEM data: Methodology and synthetic studies for resolving thin resistive layers: Geophysics, **74**, 9–20.

Kong, F., S. E. Johnstad, T. Rosten, and H. Westerdahl, 2008, A 2.5D finite element modeling difference method for marine CSEM modeling in stratified anisotropic media: Geophysics, **73**, F9–F19.

Li, Y. and S. Constable, 2007, Two dimensional marine controlled source electromagentic modelling, Part 2: Bathymetry effects: Geophysics, **72**, WA63–WA71.

Li, Y. and K. Key, 2007, Two dimensional marine controlled source electromagentic modelling, Part 1: An adaptive finite element algorithm: Geophysics, **72**, WA51–WA62.

MacGregor, L., S. Constable, and M. Sinha, 1998, The RAMESSES experiment III: Controlled source electromagnetic sounding of the Reykjanes Ridge at 57^o 45'N: Geophysics Journal International, **135**, 772–789.

MacGregor, L., M. Sinha, and S. Constable, 2001, Electrical resistivity structure of the Valu Fa Ridge, Lau Basin, from marine controlled-source electromagnetic sounding: Geophysical Journal International, **146**, 217–236.

Mitsuhata, Y., 2000, 2-D electromagnetic modeling by finite-element method with a dipole source and topography: Geophysics, **65**, 465–475.

Newman, G. A. and D. L. Alumbaugh, 1995, Frequency-domain modelling of airborne electromagnetic responses using staggered finite differences: Geophysical Prospecting, **43**, 1021–1042.

Pridmore, D., G. W. Hohmann, S. H. Ward, and W. Sill, 1981, An investigation of finite element modeling for electrical and electromagnetic data in three dimensions: Geophysics,

46, 1009–1024.

Sadiku, M. N., 2001, Numerical techniques in electromagnetics, 2 ed.: CRC Press LLC.

SanFilipo, W. A. and G. W. Hohmann, 1985, Integral equation solution for the transcient electromagnetic response of a three-dimensional body in a conductive half-space: Geophysics, **50**, 789–809.

Schwalenberg, K., M. Haeckel, J. Poort, and M. Jegen, 2009, Evaluation of gas hydrate deposits in an active seep area using marine controlled source electromagnetics: Results from Opouawe Bank, Hikurangi Margin, New Zealand:: Marine Geology, **10.1016/j.margeo.2009.07.006**.

Schwalenberg, K., E. Willoughby, R. Mir, and R. N. Edwards, 2005, Marine gas hydrate electromagnetic signatures in Cascadia and their correlation with seismic blank zones: first break, **23**, 57–63.

Tréhu, A. M. and N. Bangs, 2001, 3-D seismic imaging of an active margin hydrate system, Oregon continental margin report of cruise TTN112: Data Report 182, Oregon State University.

Tréhu, A. M., G. Bohrmann, F. Rack, M. Torres, and Shipboard Scientific Party, 2003, Procedings ODP, Initial Reports: Available from: Ocean Drilling Program, Texas A&M University, College Station TX 77845-9547, USA, **204** [**CD-ROM**].

Tréhu, A. M., M. Torres, G. Moore, E. Suess, and G. Bohrmann, 1999, Temporal and spatial evolution of a gas hydrate bearing accretionary ridge on the Oregon continental margin: Geology, **27**, 939–942.

Unsworth, M. and D. Oldenburg, 1995, Subspace inversion of electromagnetic data: application to mid-ocean-ridge exploration: Geophysical Journal International, **123**, 161–168.

Unsworth, M., B. J. Travis, and A. D. Chave, 1993, Electromagnetic induction by a finite

electric dipole source over a 2-D earth: Geophysics, **58**, 198–214.

Ward, S. H. and G. W. Hohmann, 1987, Electromagnetic methods in applied geophysics, volume **1** *of* Investigations in Geophysics, chapter 4 Electromagnetic Theory for Geophysical Applications, 131–311. Society of Exploration Geophysicists.

Weitemeyer, K., 2008, Marine electromagnetic methods for gas hydrate characterization: PhD thesis, University of California, San Diego.

Weitemeyer, K., S. Constable, K. Key, and J. Behrens, 2006, First results from a marine controlled-source electromagnetic survey to detect gas hydrates offshore Oregon: Geophysical Research Letters, **33**, doi:10.1029/2005GL024896.

Yuan, J. and R. N. Edwards, 2000, The assessment of marine gas hydrates through electronic remote sounding: Hydrate without a BSR?: Geophysical Research Letters, **27**, 2397–2400.

Zach, J. and K. Brauti, 2009, Methane hydrates in controlled-source electromagnetic surveys – analysis of a recent data example:: Geophysical Geophysical Prospecting, **57**, 601–614.

LIST OF FIGURES

dosection for the synthetic marine CSEM example (bottom). White dots are the data projections.

5 The data set used in the inversion plotted as electric field amplitude and unwrapped phase colored according to the site number. The corresponding electric field responses for a starting model of 1 Ωm are shown as dashed lines and the final inverse model of electric field responses for iteration 21 as solid lines. The transmitter navigational parameters are also plotted: depth, dip, angle from east, and x and y positions.

6 The starting model used for the inversion. The color scale has been saturated to allow the seawater resistivity values of 0.285 Ωm to 0.333 Ωm to be seen clearly. The grey color is representative of the 1 Ωm bathymetric half-space resistivity for the sediments. The inversion domain is marked by the black/white box, although the seawater resistivity is held fixed during the inversion. Note the vertical exaggeration.

7 RMS misfit based on 5% errors versus iteration during the inversion.

8 The inversion output for 14 of the 21 iterations.

9 The 2D inversion plotted with a resistivity scale from 0.5 to 3 Ωm. The transmitter positions are marked by the red line above the seafloor; receivers are marked and labeled. The estimated top of hydrate is marked by the white line and the seismic bottom simulating reflector is marked by a black line from Tréhu et al. (2003). The 5 Hz apparent resistivity pseudosection from Weitemeyer et al. (2006) is plotted below with the same color scale, but it is an apparent rather than true resistivity.

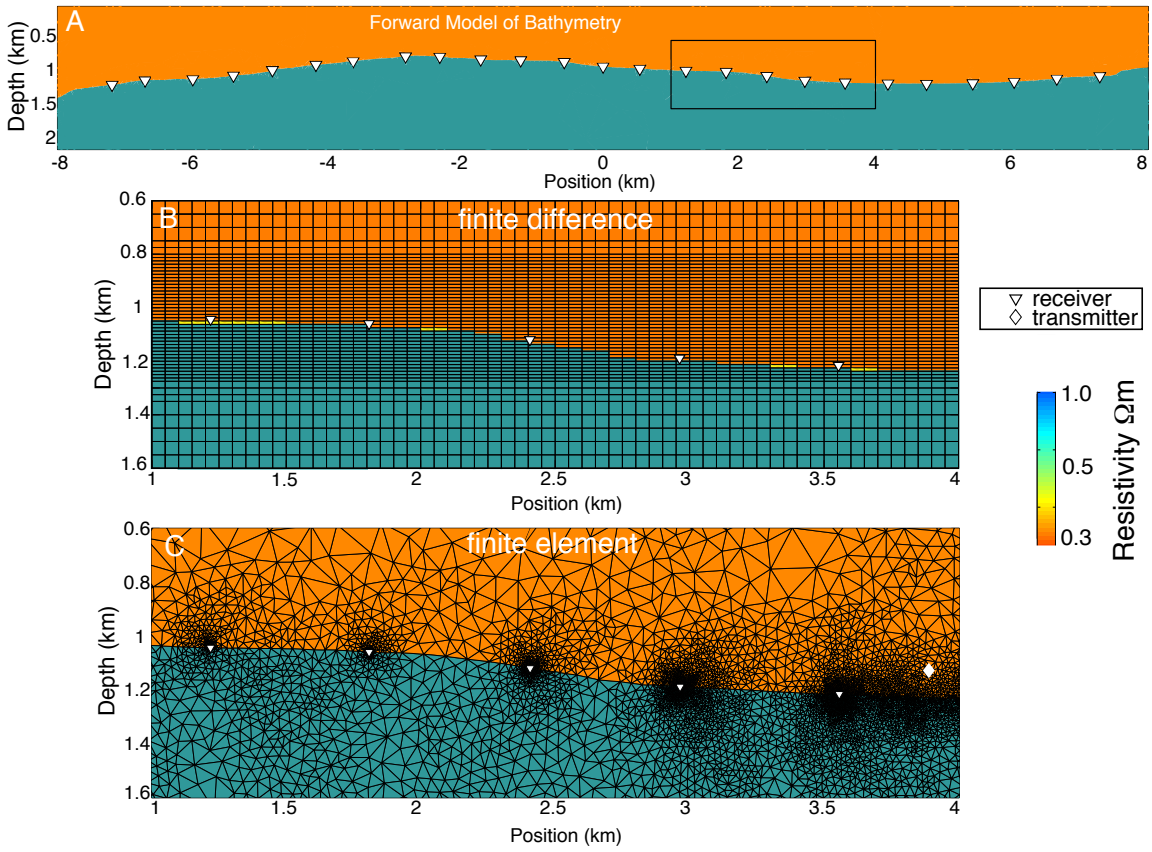

Figure 1: The bathymetry profile across HR (A) can be represented as a FD grid (B) or a FE mesh (C), where we have shown examples for the region in (A) outlined by the black box. The FE mesh has refined the model around the receivers (white triangle) and the transmitter (white diamond).

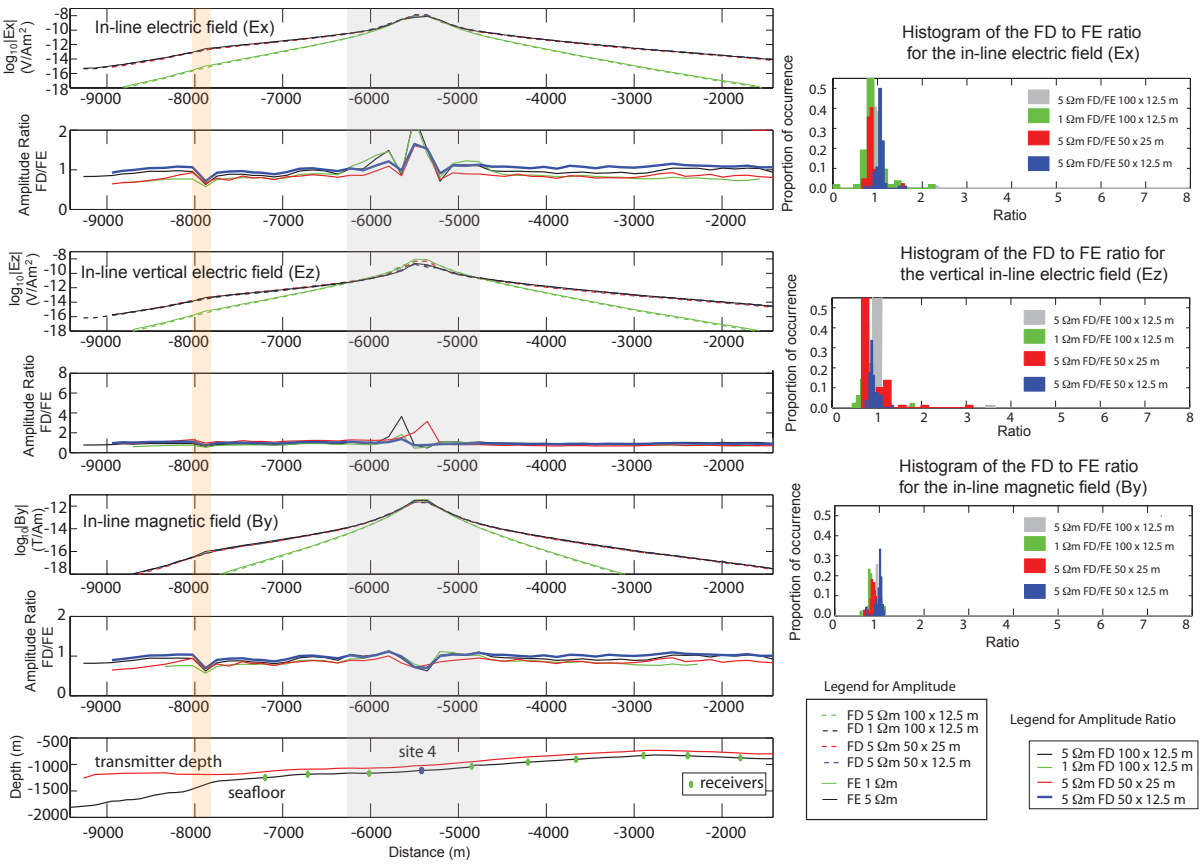

Figure 2: FE and FD log(amplitude) and amplitude ratio shown for site 4 for 3 different FD grids; 100 m by 12.5 m (at 1 Ωm and 5 Ωm), 50 m by 25 m (at 5 Ωm), and 50 m by 12.5 m (at 5 Ωm). The first six panels show the inline components of the EM field: E_x, E_z and B_y and the final panel shows the bathymetry, transmitter depth and receiver locations. To the right are histograms of the amplitude ratios for each of the FD grids modeled for E_x, E_z and B_y. The gray region shows ranges which are not used in the inversion because of saturation of the electric fields. The orange region highlights effects from bathymetry where the transmitter is just starting to attain a 100 m altitude. Note the amplitude ratio scale for the vertical component is expanded.

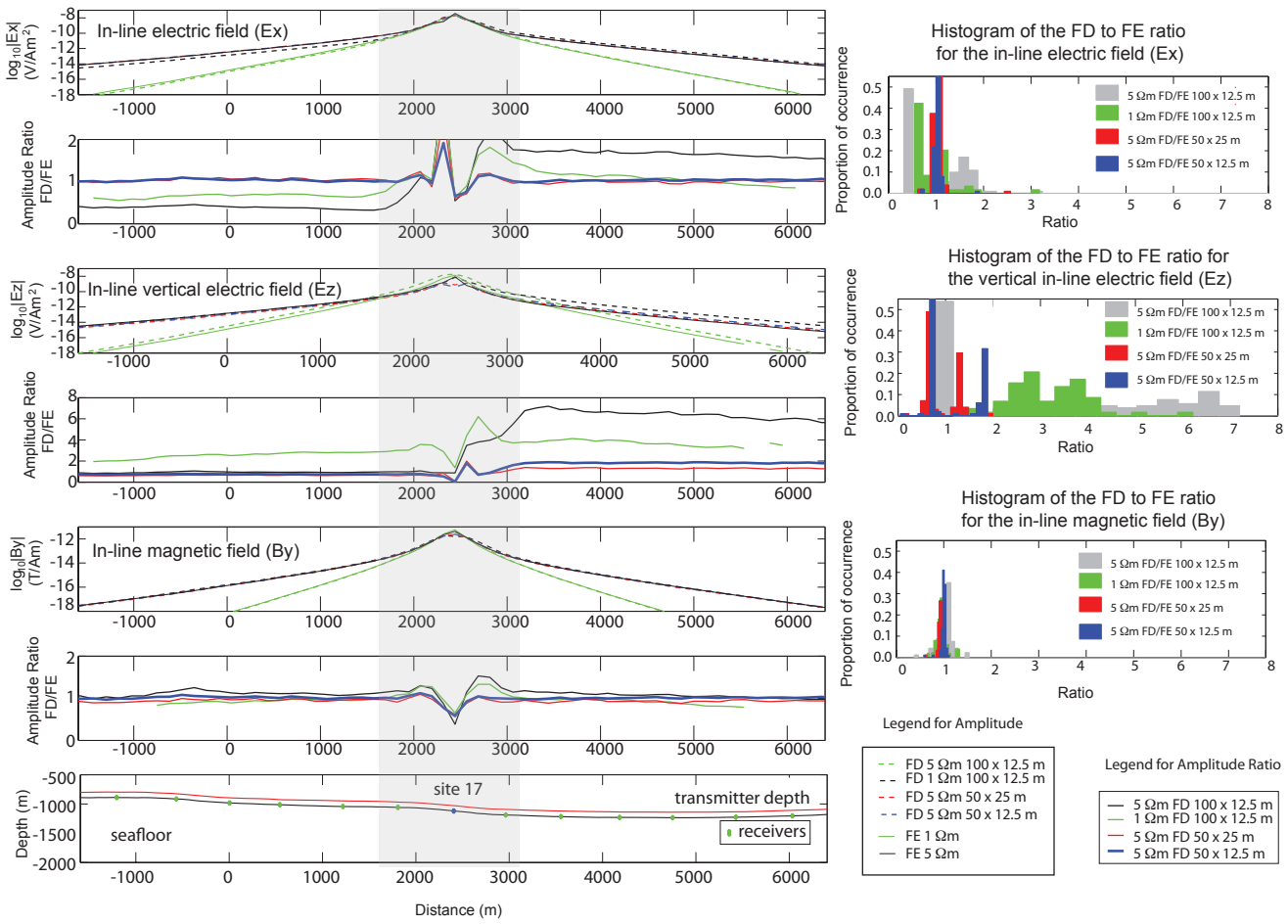

Figure 3: FE and FD log(amplitude) and amplitude ratio shown for site 17 for 3 different FD grids; 100 m by 12.5 m (at 1 Ωm and 5 Ωm), 50 m by 25 m (at 5 Ωm), and 50 m by 12.5 m (at 5 Ωm). The first six panels show the inline components of the EM field: E_x, E_z and B_y and the final panel shows the bathymetry, transmitter depth and receiver locations. To the right are histograms of the amplitude ratios for each of the FD grids modeled for E_x, E_z and B_y. The gray region shows ranges which are not used in the inversion because of saturation of the electric fields. Note the amplitude ratio scale for the vertical component is expanded.

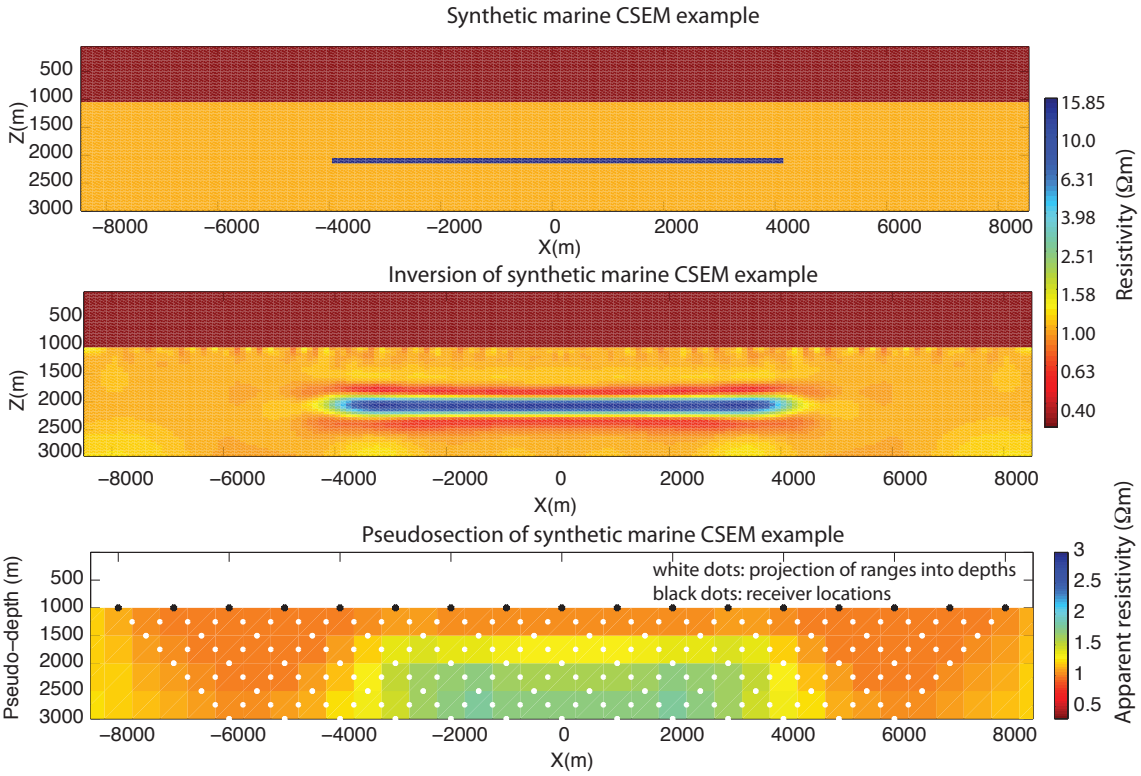

Figure 4: The synthetic marine CSEM inversion example (top). The inverted smooth resistivity model for the marine CSEM imaging example (middle). Apparent resistivity pseudosection for the synthetic marine CSEM example (bottom). White dots are the data projections.

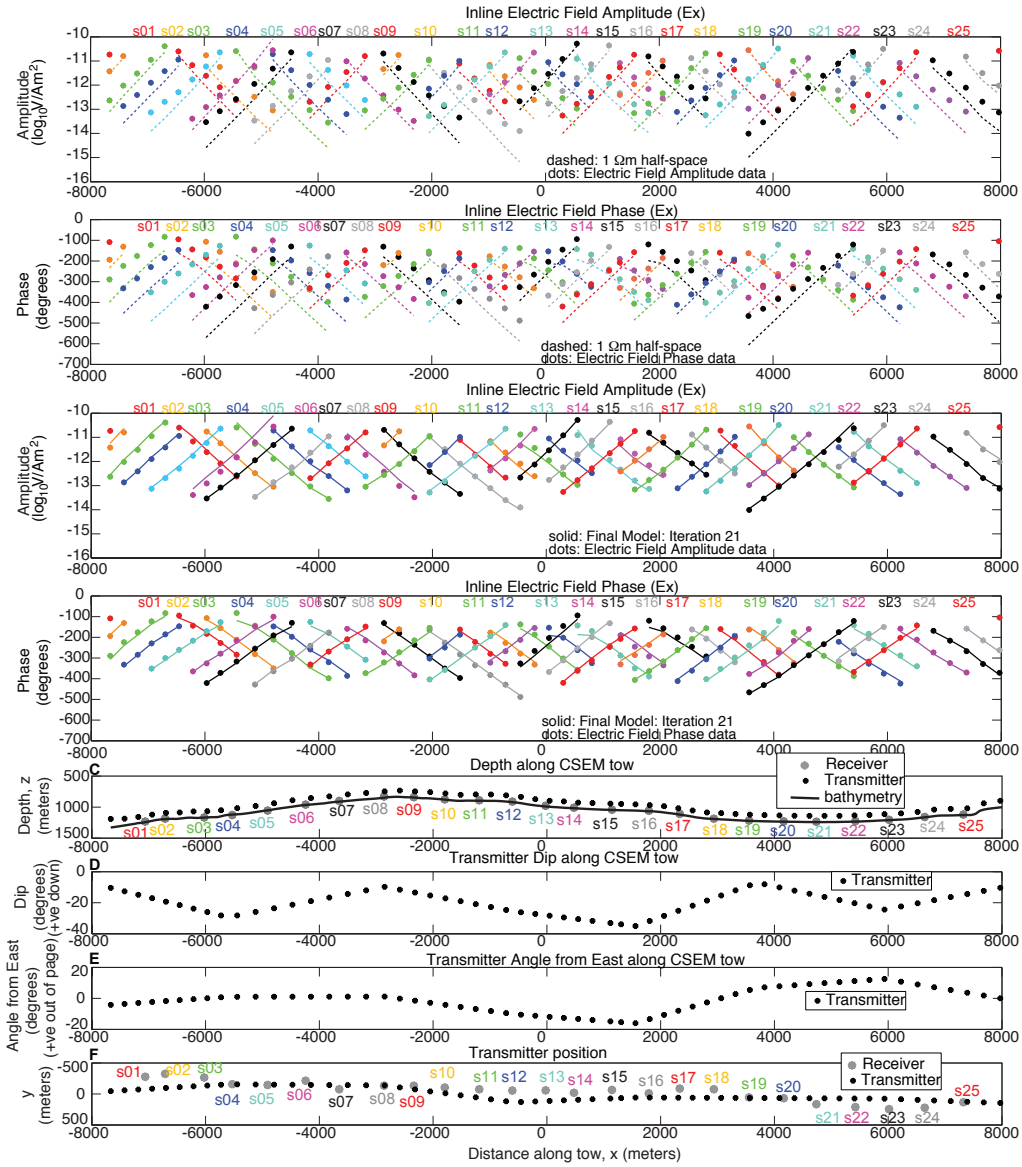

Figure 5: The data set used in the inversion plotted as electric field amplitude and unwrapped phase colored according to the site number. The corresponding electric field responses for a starting model of 1 Ωm are shown as dashed lines and the final inverse model of electric field responses for iteration 21 as solid lines. The transmitter navigational parameters are also plotted: depth, dip, angle from east, and x and y positions.

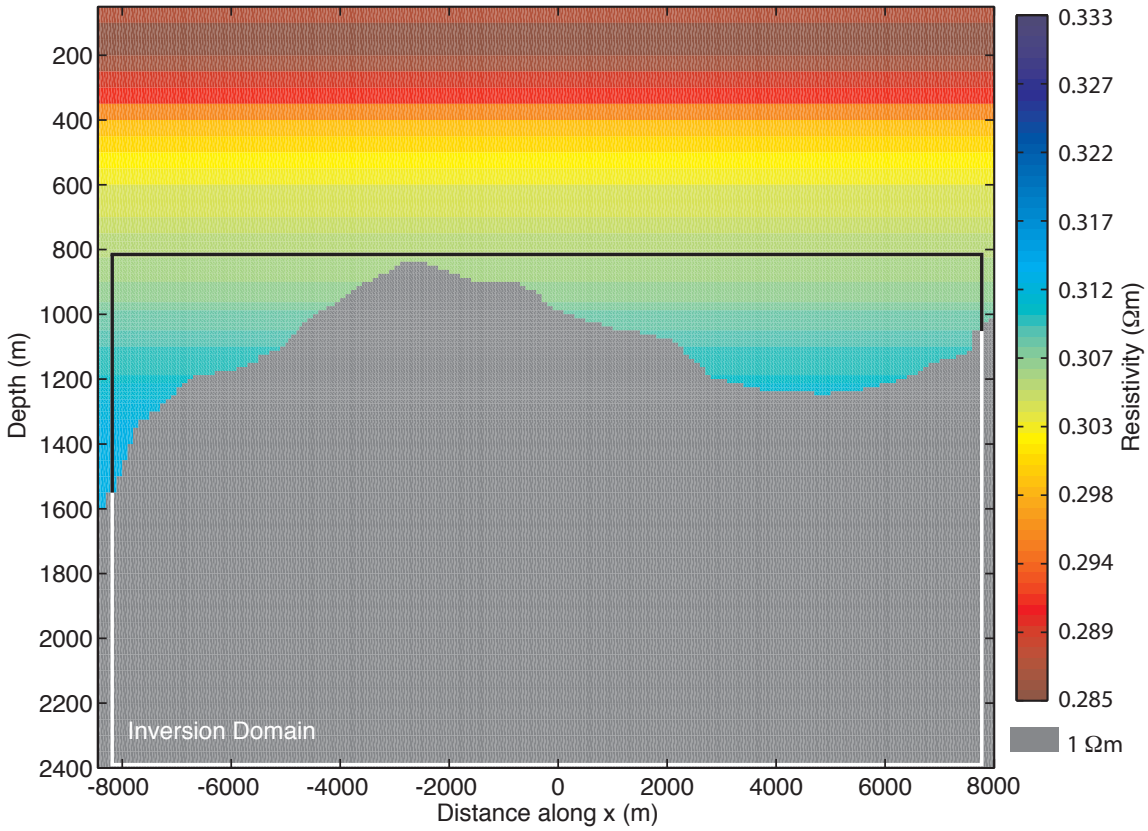

Figure 6: The starting model used for the inversion. The color scale has been saturated to allow the seawater resistivity values of 0.285 Ωm to 0.333 Ωm to be seen clearly. The grey color is representative of the 1 Ωm bathymetric half-space resistivity for the sediments. The inversion domain is marked by the black/white box, although the seawater resistivity is held fixed during the inversion. Note the vertical exaggeration.

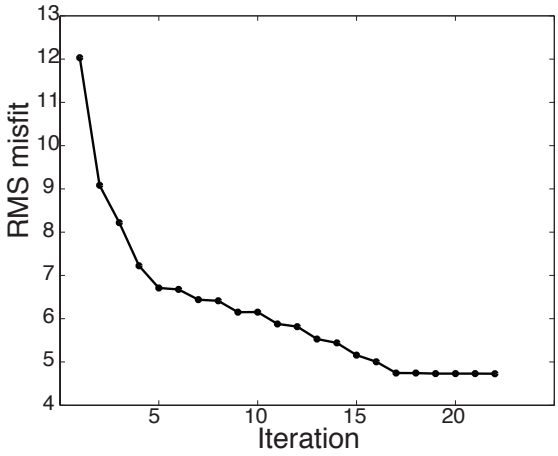

Figure 7: RMS misfit based on 5% errors versus iteration during the inversion.

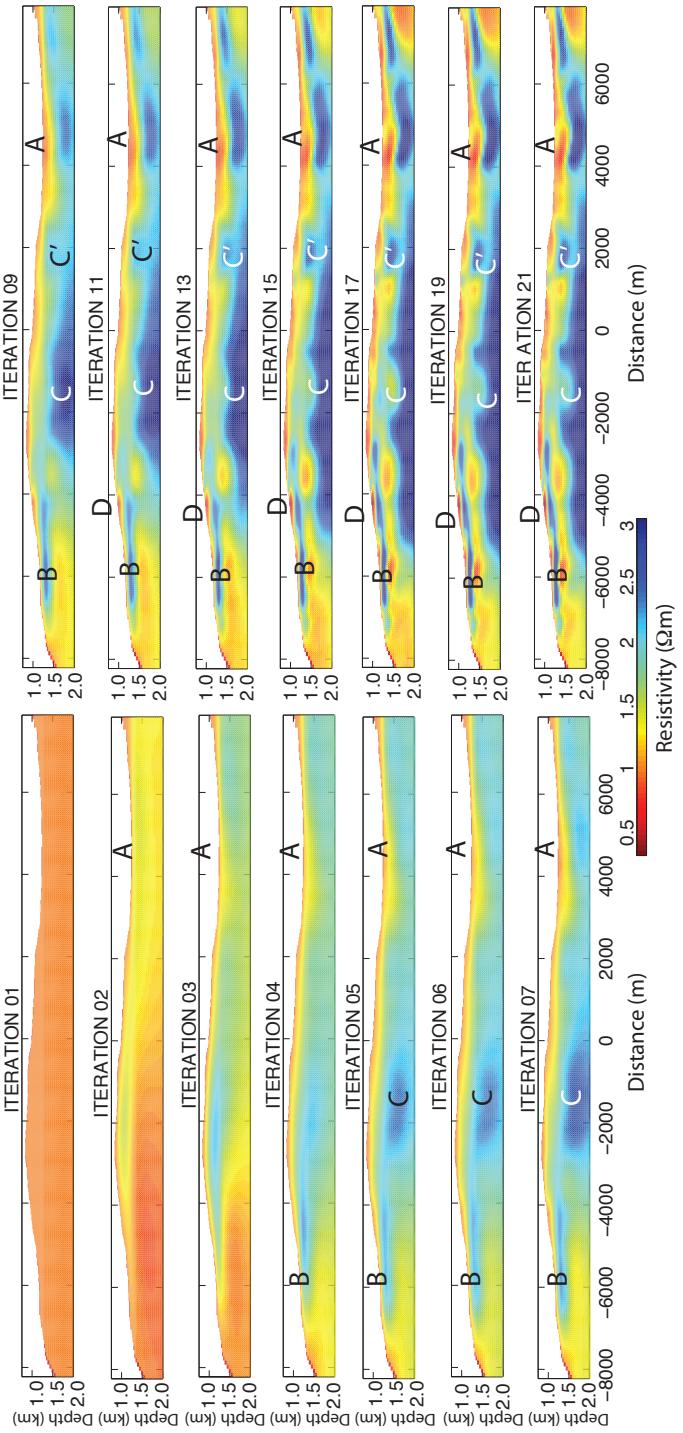

Figure 8: The inversion output for 14 of the 21 iterations.

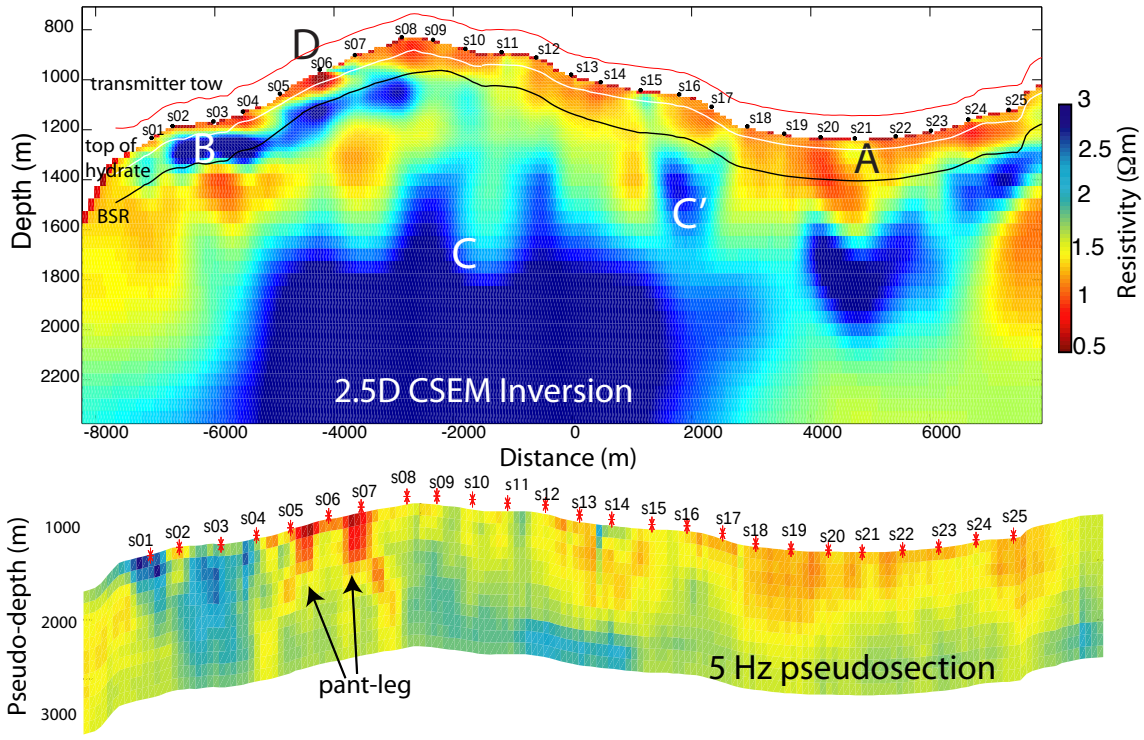

Figure 9: The 2D inversion plotted with a resistivity scale from 0.5 to 3 Ωm. The transmitter positions are marked by the red line above the seafloor; receivers are marked and labeled. The estimated top of hydrate is marked by the white line and the seismic bottom simulating reflector is marked by a black line from Tréhu et al. (2003). The 5 Hz apparent resistivity pseudosection from Weitemeyer et al. (2006) is plotted below with the same color scale, but it is an apparent rather than true resistivity.